ACS Energy LETTERS

http://pubs.acs.org/journal/aelccp

Letter

Sodium-Ion Battery Cathode with Dominating Copper and Oxygen Redox Chemistry

Arthur Ronne, Jue Liu, Yiman Zhang, Mengya Li, Seungmin Lee, Jing Wang, Gi-Hyeok Lee, Wanli Yang, Xiao-Qing Yang, Yu-chen Karen Chen-Wiegart, and Enyuan Hu*

Cite This: *ACS Energy Lett.* 2026, 11, 1827−1834

Read Online

ACCESS | Metrics & More | Article Recommendations | Supporting Information

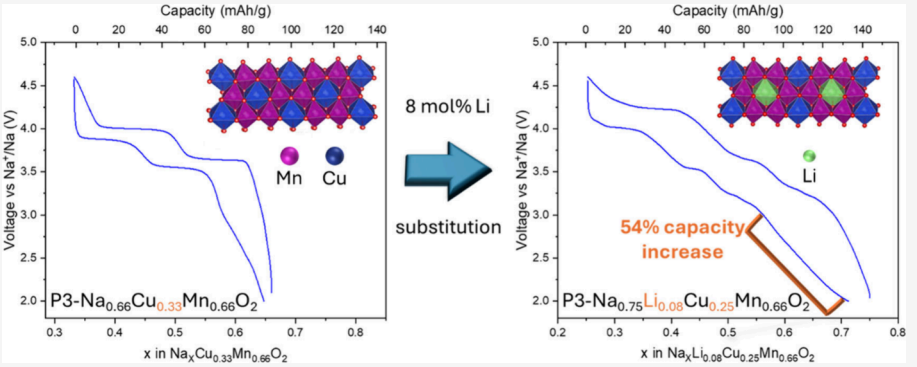

ABSTRACT: Sodium-ion batteries offer low-cost energy storage solutions for the grid and electric vehicles, leveraging the established "rocking-chair" Li-ion design and the natural abundance of sodium. However, SIBs face challenges such as relatively lower voltage and capacity than lithium-ion batteries as well as dependence on nickel resources. In this work, a new nickel-free cathode material, $Na_{0.75}Li_{0.08}Cu_{0.25}Mn_{0.66}O_2$, was designed and synthesized. This material has a capacity of ∼125 mAh/g and an average discharge voltage of 3.5 V. Notably, more than one-third of the capacity arises from lithium substitution of Cu (∼8 mol %) and high voltage activation to 4.6 V. Multimodal synchrotron X-ray characterization combining spectroscopy, microscopy, and scattering reveal the capacity is primarily from the redox of copper and oxygen, with a minor contribution from the manganese redox. Lithium substitution alters the phase transition mechanism from a two-phase transition in P3−$Na_{2/3}Cu_{1/3}Mn_{2/3}O_2$ to a solid-solution in $Na_{0.75}Li_{0.08}Cu_{0.25}Mn_{0.66}O_2$, enhancing the reversibility of this material.

Lithium-ion batteries (LIBs) are currently the dominant energy storage technology for portable electronics and electric vehicles (EV). However, the high cost and limited available resource of lithium raise concerns over larger scale applications such as grid energy storage.[1−4] Therefore, the development of inexpensive large-scale energy storage is of utmost importance. This has spurred renewed interest in sodium-ion batteries (SIBs).[5−7] Sodium is one of the most abundant elements in the Earth's crust and similar battery designs to lithium-ion can be employed.[6] Additionally, there is a wider range of transition metals including those low-cost and clean candidates such as Ti, Fe, Mn, and Cu that can be used for SIB cathode, to replace the expensive Ni and Co in LIB cathode.[8] SIB cathodes also have more structural flexibility as sodium can reside in both octahedral and prismatic sites.[9,10] However, the lower gravimetric and volumetric energy densities of sodium-ion batteries have posed challenges for the widespread adoption of this technology.

A promising approach to achieve higher-capacity positive electrode materials is to enable redox contributions from both the transition metal (TM) and oxygen, rather than relying solely on the TM. Over the past two decades, the involvement of oxygen in the redox reactions within oxide cathodes has been recognized as a mechanism for significantly increased capacity beyond that achieved by TM alone.[11−15] However, these materials typically exhibit a large voltage hysteresis during initial and subsequent cycles, and rapid voltage fade over longer-term cycling.[16] Only recently have certain materials, such as 4d and 5d transition metal cathodes,[17−19] or specific sodium cathode families[20−23] demonstrated negligible voltage hysteresis.

The theoretical rationale for reversible oxygen redox in Li-excess cathode materials for LIBs has been explored by Ceder and co-workers.[24] They have shown that oxygen coordinated

Received: October 22, 2025
Revised: December 24, 2025
Accepted: December 26, 2025
Published: January 7, 2026

https://doi.org/10.1021/acsenergylett.5c03483
ACS Energy Lett. 2026, 11, 1827−1834

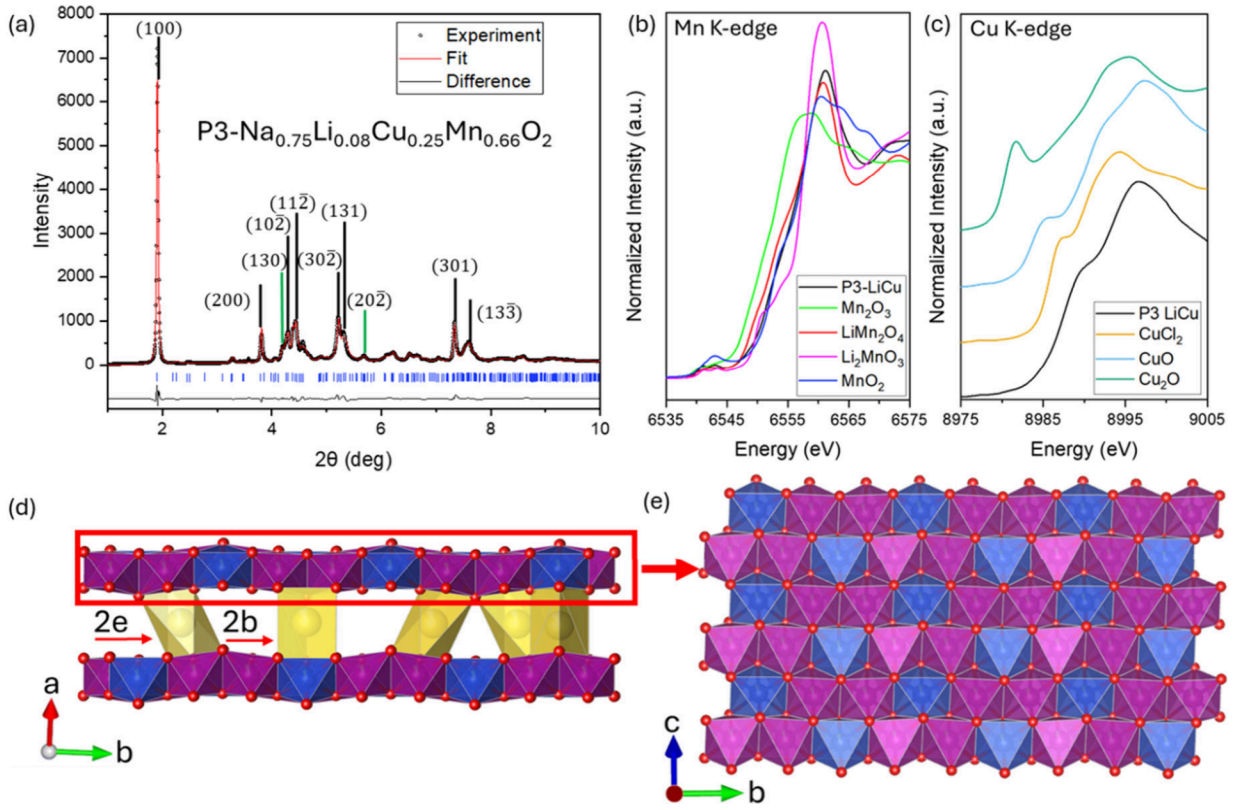

Figure 1. Pristine powder characterization. (a) Synchrotron powder XRD of P3-LiCu indexed to a $P2_1/m$ space group, with fitting result in red. Black lines are Bragg peaks from P3-LiCu and green lines are Bragg peaks from CuO. (b) Mn XANES of the pristine P3-LiCu powder with selected standards. (c) Cu XANES of the pristine P3-LiCu powder with selected standards. (d) Side view of the structure of the pristine P3-LiCu, highlighting the alternating alkali (sodium in yellow) and transition metal layers (oxygen in red, copper in blue, and manganese in purple) of this layered oxide. (e) View of the transition metal layer highlighting the honeycomb ordering.

by two TMs, instead of the conventional three (as in $LiMO_2$) leads to a nonbonding or "orphaned" 2p orbital along the Li−O−Li axis. This orphaned orbital lies just below the Fermi level and can be accessed without drawing from the Mn t_{2g} bonding orbital. These orphan orbitals can be achieved in an A−O−A configuration, where A represents an alkali metal, a vacancy, or a cation with strong ionic features (e.g., Mg^{2+}, Zn^{2+}). However, for facile substitution, Li and TM should have similar ionic radii. This requirement, in turn, leads to TM migration to other crystallographic sites upon cycling, resulting in significant structural changes, voltage hysteresis, irreversible capacity on the first cycle, and large voltage and capacity fading with extended cycling.

It has been shown that anionic redox with low hysteresis can occur in certain sodium layered oxides, namely $Na_2Mn_3O_7$[25] and sodium-deficient P2/P3-type $Na_{x<1}Li_yMn_zO_2$.[22] While the exact mechanism is still under debate, in these cases, oxidized oxygen (e.g., oxygen hole or dimer) is stable enough to be reduced in the same manner in which it was oxidized. With superstructure control, the oxidized oxygen species are stabilized through resonant π bonding. However, this low hysteresis is not preserved upon extended cycling, and novel mechanisms for stabilizing the oxygen 2p holes must be explored.

Additionally, these model systems with low hysteresis have only oxygen redox as the redox contributor and, as such, suffer from low capacity. A practical, high-capacity cathode with oxygen redox has yet to be developed. Although techniques such as doping to suppress Jahn−Teller distortion,[26] controlling molecular O_2 release,[27] utilizing of a reductive coupling mechanism,[28] and further superstructure control[29] have improved the electrochemical performance. To achieve high capacity, transition metal and oxygen redox reactions must be employed together. Recent work has shown that the p-d overlap in $Na_{2/3}Cu_{1/3}Mn_{2/3}O_2$ leads to long-term, low hysteresis oxygen and transition metal redox reactions, but the capacity is still lacking.[30]

Since its first demonstration in 2014 of the P2-type $Na_{0.68}Cu_{0.34}Mn_{0.66}O_2$,[31] which utilizes the reversible $Cu^{2+/3+}$ redox couple, copper redox has been well-explored for the SIB system.[32] Copper in the cathode has been used to develop low-cost, air-stable systems[33] that are also suitable for oxygen redox[34] systems. Recent work has demonstrated the viability of the P2−Na−Li−Cu−Mn−O system,[28,35,36] but further research into the P3 system containing Cu is lacking.

Here, we investigate the potential to combine high voltage, high capacity, and low hysteresis in a single cathode material. This combination is successfully realized in P3−$Na_{0.75}Li_{0.08}Cu_{0.25}Mn_{0.66}O_2$. The high voltage is primarily facilitated by redox reactions involving copper and oxygen, as confirmed through various spectroscopic analyses. Lithium substitution, along with high voltage activation, enables high capacity while maintaining a notably low hysteresis. The great reversibility of this material presents a promising pathway for developing nickel-free, high-energy-density sodium-ion battery cathodes.

https://doi.org/10.1021/acsenergylett.5c03483
ACS Energy Lett. 2026, 11, 1827−1834

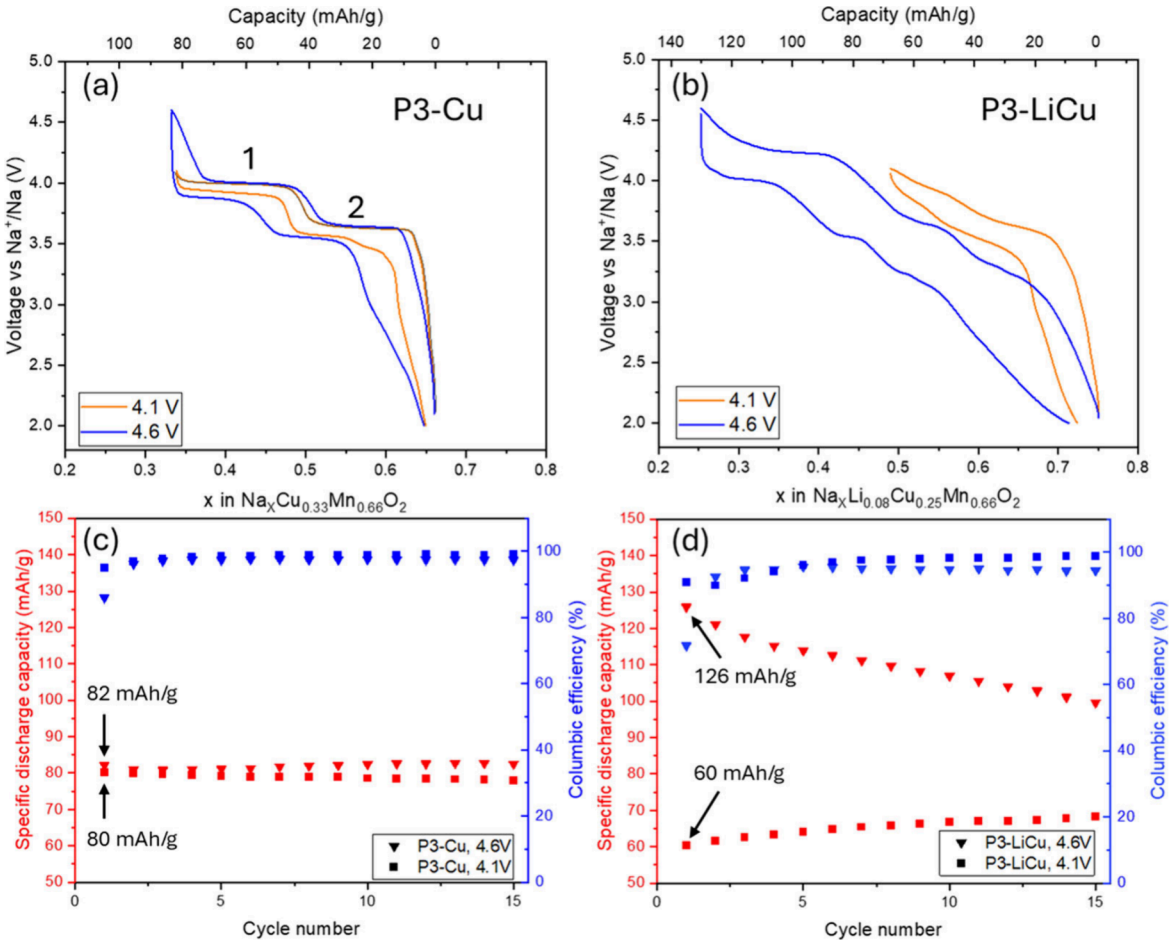

Figure 2. Galvanostatic charge−discharge cycling. (a) P3-$Na_{2/3}Cu_{1/3}Mn_{2/3}O_2$ second cycle, cycled between 2.0 and 4.1 V (blue line) or 4.6 V (orange line). (b) P3-$Na_{0.75}Li_{0.08}Cu_{0.25}Mn_{0.66}O_2$ second cycle, between 2.0 and 4.1 or 4.6 V, note the doubling of the 1st cycle discharge capacity for 4.6 V vs the 4.1 V case. (c) Cycling performance for P3-Cu at 4.1 and 4.6 V. (d) Cycling performance for P3-LiCu at 4.1 and 4.6 V. All were cycled at a 0.2C rate.

CRYSTAL STRUCTURE OF P3−$NA_{0.75}LI_{0.08}CU_{0.25}MN_{0.66}O_2$

P3−$Na_{2/3}Cu_{1/3}Mn_{2/3}O_2$ (P3-Cu) and P3−$Na_{0.75}Li_{0.08}Cu_{0.25}Mn_{0.66}O_2$ (P3-LiCu) were synthesized using a solid-state method with details described in the Method section. The reason for choosing 0.08 Li is to fully utilize the plausible redox couples in the proposed composition of $Na_{0.75}Li_{0.08}Cu_{0.25}Mn_{0.66}O_2$ while maintaining reasonable structural stability. Namely, two electrons from O^{2-} bonded to Li^+ for 0.16 total electrons and 2 electrons from the Cu^{2+} for 0.5 electrons. Compositions with 0.04 and 0.16 Li and differing Cu/Mn ratios were tested as well and are shown in Figure S1. The synchrotron X-ray diffraction (XRD) pattern of the resulting compound is shown in Figure 1a. As mentioned in previous work[30] and shown in Figure S3a, the conventional *R*3*m* space group for a P3-type cathode cannot fully index this pattern. To improve the fit, the symmetry was first reduced to a *Cm* space group to account for in-plane Cu−Mn honeycomb ordering. Next, accounting for in-plane Na-vacancy ordering further lowered the symmetry to a $P2_1/m$ space group. This monoclinic $P2_1/m$ space group indexes the pattern well, as shown in Figure 1a. Refinement[37] performed on this pattern (R_{wp} = 12) and shown in Figure 1a gives lattice parameters of a = 6.59 Å, b = 8.68 Å, c = 5.01 Å, and β = 122.10°. Additional peaks are attributed to residual CuO from the synthesis, which is refined to be 7.28% of the pristine powder. Freshly made powders under higher airflow can show CuO as low as 0.99% (Figure S2, Table S1). There are two different prismatic sites the Na can occupy, the 2e and 2b Wycoff sites, which can be seen in the a/b view of Figure 1d. A distinctive weak reflection at 2θ = 2.45° indicative of honeycomb ordering[38,39] is found (Figure S3c). The detailed refinement parameters can be found in Table S2. Therefore, the transition metal layer is honeycomb-ordered with copper in the middle of the surrounding manganese "honeycomb" (Figure 1e, Figure S3d), all in octahedral sites.

Through X-ray absorption near-edge structure (XANES), the oxidation state of a transition metal can be determined. The P3-LiCu pristine powder Mn XANES matches MnO_2, supporting the Mn is fully oxidized to Mn^{4+} in the pristine material. However, the peak at 640 eV in the total electron yield (TEY) of soft X-ray absorption spectroscopy (sXAS) in Figure S6c, the surface of the pristine material has some undercoordinated Mn, most likely Mn^{3+}, as that 640 eV peak is only seen in Mn^{2+} or Mn^{3+}. From the white line peak position (8997 eV) and shoulder peak (8990 eV), the Cu XANES spectra of the pristine P3-LiCu in Figure 1c most matches with $CuCl_2$. CuO and $CuCl_2$ both have copper in the 2+ state, however $CuCl_2$ resides in an octahedral environment while CuO resides in a square-planar environment. This matching to

https://doi.org/10.1021/acsenergylett.5c03483
ACS Energy Lett. 2026, 11, 1827−1834

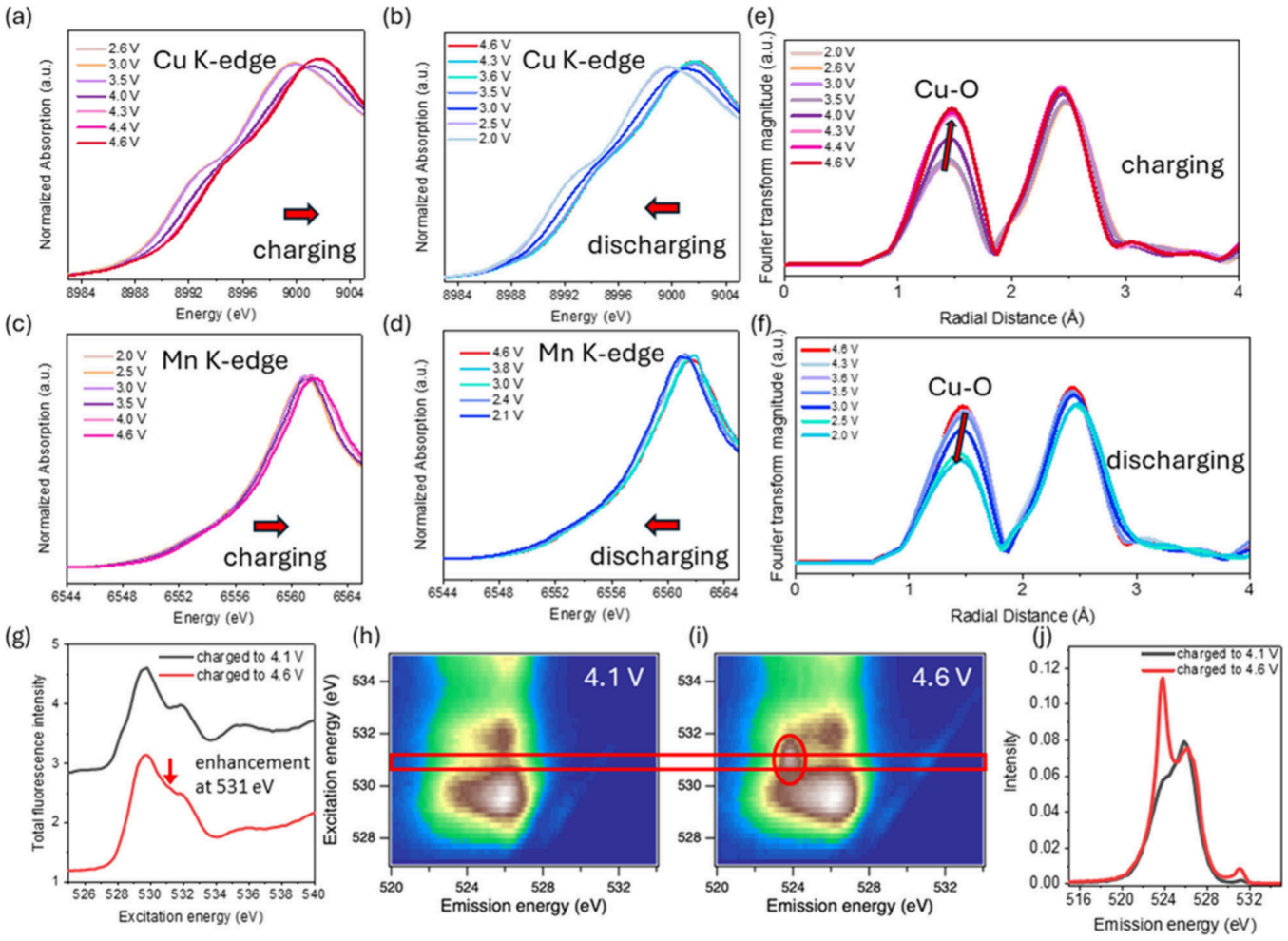

Figure 3. Redox present in P3-LiCu. (a, b) Copper K-edge XANES, peak shifts corresponding to the Cu oxidation during charging (a) or the Cu reduction during discharging (b). (c, d) Mn K-edge XANES showing minor shifts during charging (c) and discharging (d). (e, f) R-space of the Cu K-edge XAS on charge (e) and discharge (f). (g) Soft XAS at the oxygen K-edge in total fluorescence mode. (h–j) Oxygen K-edge RIXS at 4.1 V (h) with no oxidized oxygen peak and at 4.6 V (i) with the oxidized oxygen peak circled in red. The red box refers to the integration area used for (j). (j) An integration of excitation energy from 530.9 to 531.3 eV further highlighted the intensity peak at 524 eV, which is due to oxidized oxygen species.

$CuCl_2$ verifies that Cu starts in the 2+ state and resides in the octahedral environment, confirming that Cu is in the TM/Li plane. The as-synthesized particles have square facets and are cuboid generally between 5 and 10 μm in diameter, as shown by synchrotron transmission X-ray microscopy (TXM) in Figure S4 and by scanning electron microscopy in Figure S5. It should be noted that these cuboid particles are typical of polycrystalline secondary agglomerates formed during solid-state synthesis, rather than single crystals. While such polycrystalline morphology is advantageous for conventional powder processing, the internal grain boundaries and relatively large interfacial area in contact with the liquid electrolyte can promote microcracking, surface reconstruction, and parasitic reactions under high-voltage cycling. Additionally, a species with higher X-ray absorption is identified in the tomography measured at the energy above the Cu K-edge, which enhances the Cu contrast. This species is the residual CuO from synthesis, and the amount of CuO particles are similar in the pristine vs 10th cycle sample, indicating no reaction of the CuO (Figure S4).

HIGH VOLTAGE, HIGH CAPACITY, LOW HYSTERESIS P3-LICU

The electrochemical performances of both P3-Cu and P3-LiCu in half cells is shown in Figure 2. The theoretical capacity of P3-LiCu or P3-Cu is 197 mAh/g (0.75 Na) or 169 mAh/g (0.66 Na), respectively. However, this is not realized by conventional means, as deintercalation of all Na would collapse the structure, making the electrochemical reaction totally irreversible. When cycled from 2.0 V to 4.1 V at 0.2C the second cycle discharge capacities for both P3-Cu and P3-LiCu are roughly similar, which are 60 and 80 mAh/g respectively (Figure 2c,d). The 4.1 V P3-LiCu capacity is lower due to the lower Cu content of the cathode, and the P3-Cu material has 32% more Cu and a 33% higher capacity at the 4.1 V cutoff. Interestingly, the electrochemical reactions differ between the Li-doped P3-LiCu and undoped P3-Cu cathode. Two distinct plateaus are present at 4.0 and 3.6 V in the P3-Cu case, labeled 1 and 2 in Figure 2a, responsible for ~32 and 25 mAh/g capacity respectively on discharge. The presence of these distinct plateaus infers a two-phase reaction mechanism for P3−Cu. Contrarily, the P3-LiCu has an overall sloping curve, which is indicative of a solid solution mechanism when cycled

https://doi.org/10.1021/acsenergylett.5c03483
ACS Energy Lett. 2026, 11, 1827−1834

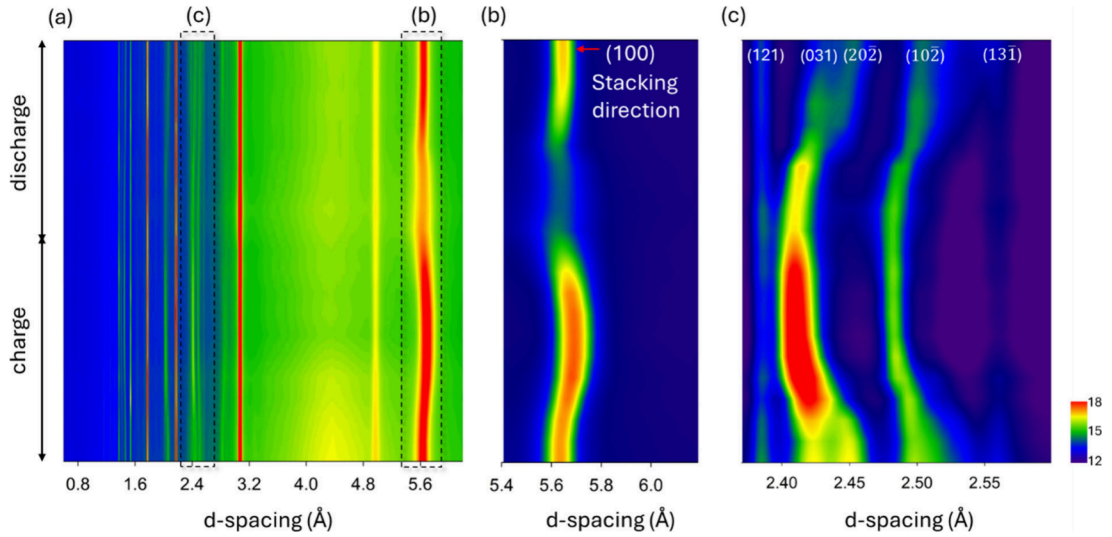

Figure 4. In-situ XRD. (a) The in situ XRD pattern between 0.7 and 3 Å. (b) Zoomed in region of interest (ROI) highlighting the (100) direction which corresponds to the a direction, which is the stacking direction in this material. (c) Zoomed in ROI, highlighting the changing ($10\bar{2}$) and (031). For the exact voltages and linescans, the reader is referred to Figure S12.

from 2.0 V to 4.1 V (Figure 2b). Several small plateaus appear when the upper cutoff voltage is raised to 4.6 V, but the overall shape remains a sloping curve. Upon further cycling, there is voltage fade in all conditions, with P3-LiCu to 4.6 V experiencing the worst (Figure S7a–d). Additionally, the 4.0 V plateau in 4.6 V P3-LiCu gradually shrinks, contributing to the capacity decay (Figure S7d). To provide more information about the electrochemistry present, dQ/dV analysis was performed, which better shows the location of the charge/discharge peaks (Figure S8). There is also a notable first cycle capacity increase of ∼25 mAh/g as the lithium molar percentage is increased from 0.04 to 0.16 (Figure S9).

There is a remarkable increase in the discharge capacity from 60 to 126 mAh/g (110% increase) for P3-LiCu when the upper bound of the cycling voltage is increased from 4.1 to 4.6 V (Figure 2b,d). Additionally, the 0.04 Li material has 102 mAh/g, and the 0.16 Li material has 125 mAh/g first cycle discharge capacity (Figure S9). This is not observed in the undoped P3-Cu, which only increases from 80 to 82 mAh/g from 4.1 to 4.6 V. From the charge–discharge profiles in Figure 2b, it is clear this extra capacity arises from a new redox couple at 4.3 V on charge and 4.0 V on discharge, with ∼0.2–0.3 V of hysteresis throughout. To understand the origin of this extra capacity and the redox mechanism of the P3-LiCu cathode, a series of X-ray spectroscopy techniques were used to characterize the material.

COPPER AND OXYGEN REDOX

First, to understand the elements and mechanisms responsible for the capacity of P3-LiCu, *operando* X-ray absorption spectroscopy (XAS) at the Cu and Mn K-edges was carried out. The origin of the capacity below 4.3 V during charge and discharge is elucidated by *operando* copper K-edge XANES shown in Figure 3a,b. The second cycle data is used, as the first cycle has formation stages not seen in later cycles. Starting at 2.6 V, the white line intensity from 8994 to 9002 eV indicates the copper is in the Cu(II) state.[40] The edge position and XANES features are constant, indicating no oxidation state change of the copper, until 3.5 V where the peak shifts higher in energy with raising voltage until 4.3 V, indicating oxidation of the copper to Cu(III) between 3.5 and 4.3 V. As shown in Figure 3b during the subsequent discharge, from 4.6 to 3.5 V, the Cu XANES is unchanged. This implies that the copper is not responsible for any discharge capacity >4.0 V in Figure 2b, alluding to there being a different mechanism responsible for the high voltage capacity. The discharge capacity that copper is responsible for is from 3.6 to 3.0 V and corresponds to ∼41 mAh/g. Cu's redox behavior is similar to the nonsubstituted material P3-$Na_{2/3}Cu_{1/2}Mn_{2/3}O_2$ that we studied in the previous case. Additionally, the Cu has little contribution to any surface reactions, supported by little change for Cu L-edge total electron yield (TEY) soft X-ray absorption spectroscopy (sXAS) in Figure S6.

The *operando* Mn K-edge XANES spectra in Figure 3c,d indicate that Mn is responsible for some of the capacity given at lower voltage (<3.25 V). There is a small shift to higher energy of the peak from 2.0 to 3.25 V on charging as some Mn^{3+} is oxidized to Mn^{4+}, and a shift to lower energy on discharge from 3.0 to 2.0 V as Mn^{4+} is reduced to Mn^{3+}, corresponding to ∼40 mAh/g. The same spectra shown in Figure 3c,d with added Mn standards can be found in a,b. The Mn likely becomes redox active because of oxygen loss as a result of activated oxygen redox which will be discussed later in this paper. Additionally, when oxygen loss occurs, it occurs at the surface first, which leads to a reduction in the surface Mn, as shown by the change in the discharged Mn L-edge TEY sXAS in Figure S6.

Quantitative extended X-ray absorption fine structure (EXAFS) modeling on substituted materials (P3-LiCu) with vacancies is challenging, but qualitative information can still be gained from the copper K-edge in r-space (Figure 3e,f). For a conventional cathode, the transition metal–oxygen bond becomes more disordered during charge, and the intensity of the first peak in the EXAFS spectra weakens as a result. However, in P3-LiCu, this peak intensifies during charge. This is because Cu starts with Cu (II) which is Jahn–Teller active and the Cu–O bond is disordered in the pristine material. As Cu is oxidized from Cu (II) to Cu (III), the Jahn–Teller distortion is removed and the CuO_6 octahedra become more ordered, leading to the Cu–O peak intensity growth.

https://doi.org/10.1021/acsenergylett.5c03483
ACS Energy Lett. 2026, 11, 1827–1834

Interestingly, such growth stopped at around 4.3 V, suggesting that a different reaction mechanism took over after that voltage. During discharge, the Cu−O peak changes in a reversible way, gradually weakening in the lower voltage region.

To understand the origin of the high voltage capacity, we resort to oxygen K-edge resonant inelastic X-ray scattering (RIXS), which has been shown to be uniquely capable of identifying a complicated redox mechanism. The emergence of a feature at 523.7 eV emission energy and 531.0 eV excitation energy is indicative of nondivalent oxygen, i.e., oxidized oxygen, as this feature can only arise when there is a partially unoccupied O-2p orbital.[41] As shown in Figure 3h at 4.1 V, the P3-LiCu has no intensity at this (523.7, 531.0) area; however, at 4.6 V this area has a strong intensity (Figure 3i). The integration of RIXS cuts from [530.9, 531.3 eV] of excitation energy and further visualizes this intensity difference at 523.7 eV (Figure 3j). Henceforth, at 4.1 V there is no oxidized oxygen, but at 4.6 V there is oxidized oxygen. Therefore, the high voltage plateau is due to oxygen redox. However, this evidence alone does not identify the reaction mechanism or the chemical state of the oxidized oxygen species.

STRUCTURAL CHANGES DURING CYCLING

Operando synchrotron XRD data were collected to observe the structural evolution during the charge and discharge phases of the first cycle (Figure 4). Overall, as seen in Figure 4, there was shifting of peaks, but there was not any appearance of new peaks. Figure S12a,b has the larger 2θ and lattice d-space ranges, further reinforcing no new peak appearances. Upon charge, the $(20\bar{2})$ peak shifts to lower d-spacing until it overlaps with the (031), and upon discharge shifts back to higher d-spacing, as seen in Figure S7c. This all suggests the P3-LiCu was able to cycle without any phase changes, a positive contribution to the overall stability of the material and has been seen in other Li-doped materials.[42,43]

With the monoclinic $P2_1/m$ space group, the stacking direction is the a direction so the (100), and (200) reflections are representative (Figure 1a, Figure S12c). Upon charging, the (100) reflection shifts to higher d-space from the start at 3.6 V (5.635 Å) to 4.16 V (5.690 Å), indicating a 0.055 Å expansion of the NaO_6 slab distance (Figure 4b). Interestingly, from 4.16 to 4.42 V the (100) reflection shifts 0.064 Å lower to 5.626 Å and broadens substantially. Upon discharging, the (100) reflection stays broadened until 3.04 V. Following, from 3.04 to 2.0 V the reflection shifts to higher d-spacing, and at 2.0 V the (100) peak position corresponds to a slightly higher d-spacing (5.646 Å) than the initial value. A similar pattern is observed in the (200) reflection (Figure S12c). Peak broadening in diffraction can occur from small grain size, instrumental broadening, or nonuniform strain. Instrumental broadening is minimal for the synchrotron source; grain size decreasing to nanoscale is unlikely to occur, so the most likely rationale is nonuniform strain of the lattice.

In contrast, the (031) (Figure 4c) reflection which has no influence from the a-direction, only the b and c-directions, shift to a smaller d-spacing from 3.72 to 4.6 V, and returns upon discharge. Additionally, the $(10\bar{2})$ and $(20\bar{2})$ (Figure 4c) reflections both shift lower upon charge and return upon discharge, while the (121) and $(13\bar{1})$ reflections (Figure 4c) stay mostly constant.

CONCLUSION

In conclusion, we have demonstrated the ability of copper to participate in low-hysteresis and reversible oxygen redox reactions at the cathode and highlighted the substantial effect of lithium doping coupled with a higher voltage. Our material is inspired by vast research into superconducting copper oxides, which has led us to employ a Zhang-Rice-like singlet state to stabilize the oxygen hole. Lithium doping is vital to achieve labile oxygen 2p orbitals and activate participation of oxygen in the redox reactions. A solid-solution mechanism improves cycling capability, as evidenced by the highly reversible structural changes shown by *operando* XRD. The redox contributions were identified from oxygen (4.0−4.6 V) by RIXS, copper (<4.0 V) and manganese (<3.0 V) by *operando* Cu and Mn K-edge XAS. Further studies to explore the unique valence and orbital interactions of copper and oxygen will be important to develop a fundamental understanding and design new cathodes with higher capacity and more stable oxygen redox.

It is noted that besides the compositional and electronic-structure tuning demonstrated here, microstructural engineering offers a complementary route to further stabilize high-voltage oxygen redox. Recent studies on single-crystalline layered oxide cathodes have shown that eliminating grain boundaries and reducing the active surface area in contact with electrolyte can mitigate microcracking, surface reconstruction, and parasitic reactions at high cutoff voltages.[44] Translating the present P3-$Na_{0.75}Li_{0.08}Cu_{0.25}Mn_{0.66}O_2$ composition and Cu/O redox mechanism into single-crystalline or otherwise crack-resistant morphologies may therefore further suppress microstructural degradation and help maintain the ∼4.3 V oxygen redox plateau over long-term cycling.

ASSOCIATED CONTENT

Supporting Information

The Supporting Information is available free of charge at https://pubs.acs.org/doi/10.1021/acsenergylett.5c03483.

Detailed experimental methods, additional data and figures including Rietveld refinement parameters, TXM and SEM images, further XRD data on varying Li/Cu/Mn content, XAS results, and electrochemical tests (PDF)

AUTHOR INFORMATION

Corresponding Author

Enyuan Hu − *Chemistry Division, Brookhaven National Laboratory, Upton, New York 11973, United States; Department of Materials Science and Chemical Engineering, Stony Brook University, Stony Brook, New York 11790, United States;* orcid.org/0000-0002-1881-4534; Email: enhu@bnl.gov

Authors

Arthur Ronne − *Chemistry Division, Brookhaven National Laboratory, Upton, New York 11973, United States; Department of Materials Science and Chemical Engineering, Stony Brook University, Stony Brook, New York 11790, United States;* orcid.org/0000-0001-7507-0757

Jue Liu − *Neutron Scattering Division, Oak Ridge National Laboratory, Oak Ridge, Tennessee 37871, United States;* orcid.org/0000-0002-4453-910X

https://doi.org/10.1021/acsenergylett.5c03483
ACS Energy Lett. 2026, 11, 1827−1834

Yiman Zhang − *Neutron Scattering Division, Oak Ridge National Laboratory, Oak Ridge, Tennessee 37871, United States*

Mengya Li − *Neutron Scattering Division, Oak Ridge National Laboratory, Oak Ridge, Tennessee 37871, United States;* orcid.org/0000-0002-9581-4044

Seungmin Lee − *Chemistry Division, Brookhaven National Laboratory, Upton, New York 11973, United States*

Jing Wang − *Chemistry Division, Brookhaven National Laboratory, Upton, New York 11973, United States; Department of Materials Science and Chemical Engineering, Stony Brook University, Stony Brook, New York 11790, United States*

Gi-Hyeok Lee − *Advanced Light Source, Lawrence Berkeley National Laboratory, Berkeley, California 94720, United States*

Wanli Yang − *Advanced Light Source, Lawrence Berkeley National Laboratory, Berkeley, California 94720, United States;* orcid.org/0000-0003-0666-8063

Xiao-Qing Yang − *Chemistry Division, Brookhaven National Laboratory, Upton, New York 11973, United States;* orcid.org/0000-0002-3625-3478

Yu-chen Karen Chen-Wiegart − *Department of Materials Science and Chemical Engineering, Stony Brook University, Stony Brook, New York 11790, United States; National Synchrotron Light Source II, Brookhaven National Laboratory, Upton, New York 11973, United States;* orcid.org/0000-0003-4445-2159

Complete contact information is available at: https://pubs.acs.org/10.1021/acsenergylett.5c03483

Notes

The authors declare no competing financial interest.

■ ACKNOWLEDGMENTS

The work conducted at Brookhaven National Laboratory was supported by the Assistant Secretary for Energy Efficiency and Renewable Energy, Vehicle Technologies Office of the U.S. Department of Energy through the Advanced Battery Materials Research (BMR) Program, including the LENS Consortium under contract no. DE-SC0012704. This research used resources and beamlines 7-BM (QAS), 28-ID-2 (XPD), 18-ID (FXI), and 23-ID-2 (IOS) of the National Synchrotron Light Source II, a U.S. Department of Energy (DOE) Office of Science User Facility operated for the DOE Office of Science by Brookhaven National Laboratory under Contract No. DE-SC0012704. The Advanced Light Source is supported by the Director, Office of Science, Office of Basic Energy Sciences, of the US Department of Energy under contract no. DE-AC02-05CH11231.

■ REFERENCES

(1) Armand, M.; Tarascon, J. M. Building better batteries. *Nature* **2008**, *451* (7179), 652−657.

(2) Challenge, E. S. G. *Energy Storage Market Report*; US Department of Energy, 2020.

(3) Swain, B. Recovery and recycling of lithium: A review. *Sep. Purif. Technol.* **2017**, *172*, 388−403.

(4) Zu, C.-X.; Li, H. Thermodynamic analysis on energy densities of batteries. *Energy Environ. Sci.* **2011**, *4* (8), 2614.

(5) Kubota, K.; Komaba, S. Review—Practical Issues and Future Perspective for Na-Ion Batteries. *J. Electrochem. Soc.* **2015**, *162* (14), A2538−A2550.

(6) Yabuuchi, N.; Kubota, K.; Dahbi, M.; Komaba, S. Research development on sodium-ion batteries. *Chem. Rev.* **2014**, *114* (23), 11636−11682.

(7) Rahman, M. M.; Lin, F. Oxygen Redox Chemistry in Rechargeable Li-Ion and Na-Ion Batteries. *Matter* **2021**, *4* (2), 490−527.

(8) Yan, Z.; Tang, L.; Huang, Y.; Hua, W.; Wang, Y.; Liu, R.; Gu, Q.; Indris, S.; Chou, S. L.; Huang, Y.; et al. A Hydrostable Cathode Material Based on the Layered P2@P3 Composite that Shows Redox Behavior for Copper in High-Rate and Long-Cycling Sodium-Ion Batteries. *Angew. Chem.* **2019**, *131* (5), 1426−1430.

(9) Su, H.; Jaffer, S.; Yu, H. Transition metal oxides for sodium-ion batteries. *Energy Storage Mater.* **2016**, *5*, 116−131.

(10) Liu, Q.; Hu, Z.; Chen, M.; Zou, C.; Jin, H.; Wang, S.; Chou, S. L.; Dou, S. X. Recent progress of layered transition metal oxide cathodes for sodium-ion batteries. *Small* **2019**, *15* (32), 1805381.

(11) Yoon, W.-S.; Kim, K.-B.; Kim, M.-G.; Lee, M.-K.; Shin, H.-J.; Lee, J.-M.; Lee, J.-S.; Yo, C.-H. Oxygen Contribution on Li-Ion Intercalation-Deintercalation in $LiCoO_2$ Investigated by O K-Edge and Co L-Edge X-ray Absorption Spectroscopy. *J. Phys. Chem. B* **2002**, *106* (10), 2526−2532.

(12) Dahéron, L.; Dedryvère, R.; Martinez, H.; Ménétrier, M.; Denage, C.; Delmas, C.; Gonbeau, D. Electron Transfer Mechanisms upon Lithium Deintercalation from $LiCoO_2$ to CoO_2 Investigated by XPS. *Chem. Mater.* **2008**, *20* (2), 583−590.

(13) Lu, Z.; Dahn, J. R. Understanding the Anomalous Capacity of Li/Li[Ni $_x$Li $_{(1/3-2x/3)}$Mn $_{(2/3-x/3)}$]O_2 Cells Using In Situ X-Ray Diffraction and Electrochemical Studies. *J. Electrochem. Soc.* **2002**, *149* (7), A815.

(14) Luo, K.; Roberts, M. R.; Hao, R.; Guerrini, N.; Pickup, D. M.; Liu, Y.-S.; Edström, K.; Guo, J.; Chadwick, A. V.; Duda, L. C.; et al. Charge-compensation in 3d-transition-metal-oxide intercalation cathodes through the generation of localized electron holes on oxygen. *Nat. Chem.* **2016**, *8* (7), 684−691.

(15) Koga, H.; Croguennec, L.; Ménétrier, M.; Mannessiez, P.; Weill, F.; Delmas, C.; Belin, S. Operando X-ray Absorption Study of the Redox Processes Involved upon Cycling of the Li-Rich Layered Oxide $Li_{1.20}Mn_{0.54}Co_{0.13}Ni_{0.13}O_2$ in Li Ion Batteries. *J. Phys. Chem. C* **2014**, *118* (11), 5700−5709.

(16) Assat, G.; Tarascon, J.-M. Fundamental understanding and practical challenges of anionic redox activity in Li-ion batteries. *Nat. Energy* **2018**, *3* (5), 373−386.

(17) Sathiya, M.; Rousse, G.; Ramesha, K.; Laisa, C. P.; Vezin, H.; Sougrati, M. T.; Doublet, M. L.; Foix, D.; Gonbeau, D.; Walker, W.; et al. Reversible anionic redox chemistry in high-capacity layered-oxide electrodes. *Nat. Mater.* **2013**, *12* (9), 827−835.

(18) McCalla, E.; Abakumov, A. M.; Saubanère, M.; Foix, D.; Berg, E. J.; Rousse, G.; Doublet, M.-L.; Gonbeau, D.; Novák, P.; Van Tendeloo, G.; et al. Visualization of O-O peroxo-like dimers in high-capacity layered oxides for Li-ion batteries. *Science* **2015**, *350* (6267), 1516−1521.

(19) Zhuo, Z.; Dai, K.; Wu, J.; Zhang, L.; Tamura, N.; Chuang, Y.-d.; Feng, J.; Guo, J.; Shen, Z.-x.; Liu, G.; et al. Distinct Oxygen Redox Activities in Li_2MO_3 (M = Mn, Ru, Ir). *ACS Energy Lett.* **2021**, *6* (10), 3417−3424.

(20) Song, B.; Tang, M.; Hu, E.; Borkiewicz, O. J.; Wiaderek, K. M.; Zhang, Y.; Phillip, N. D.; Liu, X.; Shadike, Z.; Li, C.; et al. Understanding the Low-Voltage Hysteresis of Anionic Redox in $Na_2Mn_3O_7$. *Chem. Mater.* **2019**, *31* (10), 3756−3765.

(21) Wu, Q.; Zhang, T.; Geng, J.; Gao, S.; Ma, H.; Li, F. Anionic Redox Chemistry for Sodium-Ion Batteries: Mechanisms, Advances, and Challenges. *Energy Fuels* **2022**, *36* (15), 8081−8095.

(22) Rong, X.; Liu, J.; Hu, E.; Liu, Y.; Wang, Y.; Wu, J.; Yu, X.; Page, K.; Hu, Y.-S.; Yang, W.; et al. Structure-Induced Reversible Anionic Redox Activity in Na Layered Oxide Cathode. *Joule* **2018**, *2* (1), 125−140.

(23) Du, K.; Zhu, J.; Hu, G.; Gao, H.; Li, Y.; Goodenough, J. B. Exploring reversible oxidation of oxygen in a manganese oxide. *Energy Environ. Sci.* **2016**, *9* (8), 2575−2577.

(24) Seo, D.-H.; Lee, J.; Urban, A.; Malik, R.; Kang, S.; Ceder, G. The structural and chemical origin of the oxygen redox activity in layered and cation-disordered Li-excess cathode materials. *Nat. Chem.* **2016**, *8* (7), 692−697.
(25) Adamczyk, E.; Pralong, V. $Na_2Mn_3O_7$: A Suitable Electrode Material for Na-Ion Batteries? *Chem. Mater.* **2017**, *29* (11), 4645−4648.
(26) Rahman, M. M.; McGuigan, S.; Li, S.; Gao, L.; Hou, D.; Yang, Z.; Xu, Z.; Lee, S.-J.; Sun, C.-J.; Liu, J.; et al. Chemical Modulation of Local Transition Metal Environment Enables Reversible Oxygen Redox in Mn-Based Layered Cathodes. *ACS Energy Lett.* **2021**, *6* (8), 2882−2890.
(27) Massaro, A.; Muñoz-García, A. B.; Prosini, P. P.; Gerbaldi, C.; Pavone, M. Unveiling Oxygen Redox Activity in P2-Type $Na_xNi_{0.25}Mn_{0.68}O_2$ High-Energy Cathode for Na-Ion Batteries. *ACS Energy Lett.* **2021**, *6* (7), 2470−2480.
(28) Wang, Y.; Zhao, X.; Jin, J.; Shen, Q.; Hu, Y.; Song, X.; Li, H.; Qu, X.; Jiao, L.; Liu, Y. Boosting the Reversibility and Kinetics of Anionic Redox Chemistry in Sodium-Ion Oxide Cathodes via Reductive Coupling Mechanism. *J. Am. Chem. Soc.* **2023**, *145* (41), 22708−22719.
(29) Mudassir, H. M.; Xie, C.; Xia, F.; Fang, R.; Chen, Q.; Liu, Z.; Dong, T.; Liu, F.; Hu, S.; Jian, Z.; et al. P2/P3 Biphasic layered oxide cathode enabled by additional electron-holes on oxygen for high-capacity sodium-ion batteries. *J. Mater. Sci. Technol.* **2025**, *238*, 230−237.
(30) Wang, X.; Yin, L.; Ronne, A.; Zhang, Y.; Hu, Z.; Tan, S.; Wang, Q.; Song, B.; Li, M.; Rong, X.; et al. Stabilizing lattice oxygen redox in layered sodium transition metal oxide through spin singlet state. *Nat. Commun.* **2023**, *14* (1), 7665.
(31) Xu, S.-Y.; Wu, X.-Y.; Li, Y.-M.; Hu, Y.-S.; Chen, L.-Q. Novel copper redox-based cathode materials for room-temperature sodium-ion batteries. *Chinese Physics B* **2014**, *23* (11), 118202.
(32) Mason, C. W.; Lange, F.; Saravanan, K.; Lin, F.; Nordlund, D. Beyond Divalent Copper: A Redox Couple for Sodium Ion Battery Cathode Materials. *ECS Electrochemistry Letters* **2015**, *4* (5), A41−A44.
(33) Li, Y.; Yang, Z.; Xu, S.; Mu, L.; Gu, L.; Hu, Y. S.; Li, H.; Chen, L. Air-Stable Copper-Based P2- $Na_{7/9}Cu_{2/9}Fe_{1/9}Mn_{2/3}O_2$ as a New Positive Electrode Material for Sodium-Ion Batteries. *Advanced Science* **2015**, *2* (6), 1500031.
(34) Gu, M.; Xu, J.; Shi, X.; Shao, L.; Sun, Z. Research progress of oxygen redox in sodium-layered oxides. *Battery Energy* **2024**, *3* (3), 20230046 DOI: 10.1002/bte2.20230046.
(35) Chen, Z.; Jiao, R.; Liu, H.; Wang, H.; Liu, X.; Zhang, X.; Jia, M.; Chen, Y.; Yan, X. Coupling the Electronic Distribution and Oxygen Redox Potential via Cu Substitution of Layered Oxide Cathodes for Sodium-Ion Batteries. *ACS Sustain. Chem. Eng.* **2024**, *12* (2), 816−825.
(36) Rong, X.; Xiao, D.; Li, Q.; Niu, Y.; Ding, F.; Hou, X.; Wang, Q.; Xu, J.; Zhao, C.; Zhou, D.; et al. Boosting reversible anionic redox reaction with Li/Cu dual honeycomb centers. *eScience* **2023**, *3* (5), 100159.
(37) Coelho, A. A. TOPAS and TOPAS-Academic: an optimization program integrating computer algebra and crystallographic objects written in C++. *J. Appl. Crystallogr.* **2018**, *51* (1), 210−218.
(38) Yin, W.; Huang, Z.; Zhang, T.; Yang, T.; Ji, H.; Zhou, Y.; Shi, S.; Zhang, Y. P2-type layered oxide cathode with honeycomb-ordered superstructure for sodium-ion batteries. *Energy Storage Mater.* **2024**, *69*, 103424.
(39) Yuan, D.; Liang, X.; Wu, L.; Cao, Y.; Ai, X.; Feng, J.; Yang, H. A honeycomb-layered $Na_3Ni_2SbO_6$: a high-rate and cycle-stable cathode for sodium-ion batteries. *Adv. Mater.* **2014**, *26* (36), 6301−6306.
(40) Gaur, A.; Shrivastava, B.; Joshi, S. Copper K-edge XANES of Cu (I) and Cu (II) oxide mixtures. *J. Phys. Conf. Ser.* **2009**, *190*, 012084.
(41) Zhuo, Z.; Pemmaraju, C. D.; Vinson, J.; Jia, C.; Moritz, B.; Lee, I.; Sallies, S.; Li, Q.; Wu, J.; Dai, K.; et al. Spectroscopic Signature of Oxidized Oxygen States in Peroxides. *J. Phys. Chem. Lett.* **2018**, *9* (21), 6378−6384.
(42) Yang, L.; Li, X.; Liu, J.; Xiong, S.; Ma, X.; Liu, P.; Bai, J.; Xu, W.; Tang, Y.; Hu, Y.-Y.; et al. Lithium-doping stabilized high-performance P2-$Na_{0.66}Li_{0.18}Fe_{0.12}Mn_{0.7}O_2$ cathode for sodium ion batteries. *J. Am. Chem. Soc.* **2019**, *141* (16), 6680−6689.
(43) Lian, Z.; Wang, H.; Chen, Z.; Xu, C.; Yu, H.; Ding, F.; Mao, H.; Yu, D.; Yang, Y.; Wang, B.; Zhou, L.; Zhang, J.; Zhao, X.; Zhang, Q.; Rong, X.; Shi, X.; Zhang, L.; Hu, Y.-S.; Zhao, J. High-Energy Na-Ion Batteries Using Single-Crystalline Cathode. *ACS Energy Lett.* **2025**, *10* (3), 1517−1528.
(44) Ryu, H.-H.; Lee, S.-B.; Yoon, C. S.; Sun, Y.-K. Morphology-Dependent Battery Performance of Ni-Rich Layered Cathodes: Single-Crystal versus Refined Polycrystal. *ACS Energy Lett.* **2022**, *7* (9), 3072−3079.

https://doi.org/10.1021/acsenergylett.5c03483
ACS Energy Lett. 2026, 11, 1827−1834